

An experimental investigation of planar countercurrent turbulent shear layers

By DAVID J. FORLITI†, BRIAN A. TANG
AND PAUL J. STRYKOWSKI

Department of Mechanical Engineering, University of Minnesota, Minneapolis, MN 55455, USA

(Received 27 November 2002 and in revised form 3 December 2004)

The spatial development of planar incompressible countercurrent shear layers was investigated experimentally. A facility was constructed to establish countercurrent shear layers without the formation of global stagnation in the flow. Particle image velocimetry was employed to obtain detailed measurements within the region of self-preservation for velocity ratios U_2/U_1 between 0 and -0.3 . The spatial growth rate of countercurrent shear layers was found to agree generally with simple analytical theory. At 30% counterflow, the growth rate was approximately twice as large as the case with no counterflow. Peak turbulence quantities, when normalized by the applied shear magnitude, ΔU , were found to be nominally constant for low levels of counterflow, but at counterflow velocities above 13% of the primary stream velocity, peak turbulence levels increased. The observed transition is accompanied by the development of mean flow three-dimensionality. The deviation occurs at a counterflow level that is in agreement with theoretical predictions for transition from convective to absolute instability.

1. Introduction

Turbulent shear layers have been one of the most studied shear flows for several decades. Emerging diagnostic techniques and computational methods in recent years have greatly improved our understanding of shear layers, but many aspects have yet to be understood which motivates the continuing work in this area. Additionally, certain shear layer regimes have received limited attention.

Numerous investigators have studied the dynamics of coflowing planar shear layers and round jets over the years (e.g. Spencer & Jones 1971; Brown & Roshko 1974; Rodi 1975; Dziomba & Fiedler 1985; Mehta & Westphal 1986). In contrast, the counterflowing shear layer has received relatively little attention. In fact, until the 1990s only the temporal development of the countercurrent shear layer had been studied experimentally (Thorpe 1968, 1971; Ramshankar 1988). Countercurrent shear layers are ubiquitously present in flows containing boundary-layer separation, hence are relevant to many applications.

The primary goal of this work is to carefully document for the first time the dynamics of a self-preserving planar countercurrent shear layer. A range of counterflow levels from 0% to 30% of the primary stream velocity are studied in a facility designed to minimize mean flow three-dimensionality. The results will add to the extensive

† Present address: Department of Mechanical and Aerospace Engineering, State University of New York at Buffalo, Buffalo, NY 14260, USA.

knowledge of free shear layers that has been previously examined predominantly in the coflowing regime.

2. Background

The shear-layer velocity profile is unstable at all practical Reynolds numbers (Drazin & Reid 1981). For the common spatially developing shear layer, disturbances in the base flow are amplified in the streamwise direction and undergo a transition to a fully turbulent state. At some point downstream of the origin, the turbulent shear layer should become independent of its initial conditions (Townsend 1976), i.e. reach a self-preserving, or self-similar, state. Self-similarity is a state of local equilibrium where flow quantities are only dependent upon local variables, including the primary and secondary mean velocities, shear layer width, etc. as measured at the local streamwise position. In theory, all time-averaged flow quantities such as \bar{U} , \bar{V} , u'_{rms} , v'_{rms} , $\overline{u'v'}$, and other higher-order terms should be self-preserving when properly normalized by local coordinates. Mehta & Westphal (1986) present a set of conditions that are required for self-similarity of free shear layers. Oster & Wygnanski (1982) discuss the universal self-similarity of shear layers and provide insight into sources of data scatter observed in the literature.

Not all workers follow the same guidelines for establishing similarity, and the determination is subjective even when following the same guidelines. A comprehensive review (Birch & Eggers 1972) was performed of the shear-layer literature and it was found that very few authors demonstrated similarity in turbulent quantities. They presented a comparison of growth rates by numerous investigators and found tremendous scatter. The scatter was attributed mainly to insufficient development distances in most facilities. A more recent review by Ho & Huerre (1984) describes various fundamental aspects of shear layers including turbulent structures and linear stability theory.

2.1. Countercurrent shear layers

The first systematic attempt at establishing a spatially evolving planar countercurrent shear layer was made by Humphrey & Li (1981). Their facility consisted of opposing momentum-driven streams separated by splitter plates and bounded by the walls of a closed circuit wind tunnel. While the purpose of the study was to create a mixing region between the opposing streams, the flow set up a global stagnation zone at a scale commensurate with the test section itself. Essentially, the primary and secondary streams came to rest, causing each to turn and exhaust 180° from the direction in which they entered. The global stagnation disrupted the ability of the shear to promote turbulent mixing.

Huerre & Monkewitz (1985) provided further insight into this flow as they explored the spatial-temporal stability of the planar shear layer. They discovered that the shear layer experiences a transition from convective to absolute instability when the secondary reverse stream achieves a velocity magnitude greater than approximately 13 % of the primary forward stream ($\lambda = 1.315$, $r = -0.136$ where $\lambda = (U_1 - U_2)/(U_1 + U_2)$ and $r = U_2/U_1$). The implications of this stability transition – strictly valid for parallel flows – on the development of a spatially developing flow were investigated in a laboratory setting by Strykowski & Niccum (1991, 1992).

They generated countercurrent shear in the near field of an initially laminar round jet and demonstrated the existence of a rather abrupt transition near $\lambda = 1.3$, which was in good agreement with the theoretical value predicted by Huerre & Monkewitz. Shear-layer oscillations were found at a discrete frequency as the flow set up an

inherent feedback, which is suggestive of a global instability. In the absolutely unstable regime, the typical laminar shear-layer vortex pairing in the developing region was suppressed. Consequently, the shear-layer growth was actually reduced, much as was seen in previous forcing experiments (e.g. Dziomba & Fiedler 1985).

Wilcoxon (1996) studied the dynamics of a turbulent jet with counterflow applied to the jet periphery. An extension collar was used to increase the streamwise length over which counterflow was developed. It was found that the length of the collar had a strong impact on the turbulence control in the shear layer of the jet, and the shear-layer growth increased with increased counterflow levels (Strykowski & Wilcoxon 1993).

Khemakhem (1997) was the first to attempt to study the planar countercurrent turbulent shear layer in a partially unconfined manner. Khemakhem used a momentum-driven primary stream and a suction-driven secondary stream to set up a countercurrent shear layer that did not develop the global stagnation observed by Humphrey & Li (1981). Khemakhem was able to demonstrate some basic features of the shear layer, but difficulties in using hot wires to measure flow in two streamwise directions led to uncertainties in the data. Khemakhem also constructed a smaller countercurrent facility designed to accommodate particle image velocimetry (PIV). Although a global stagnation was not found in the new facility, it was burdened by a highly three-dimensional mean flow.

While the basic features of countercurrent shear layers have been documented over a range of conditions (including jets at low and high Reynolds numbers), the basic physics of a planar countercurrent turbulent shear layer remain unexplored. The motivation for the present work was to fill this gap in our fundamental understanding of this flow.

3. Approach and instrumentation

The experiments were performed in a fan-driven wind tunnel in the Shear Flow Control Laboratory at the University of Minnesota. The primary stream is momentum driven by an Aerovent 710-BIA CBD belt-driven fan, which is powered by a 15 h.p. Toshiba electric motor. The motor speed is controlled by a Toshiba–Houston Tosvert-130 H1 transistor inverter. The air from the fan goes through a round to square diffuser section and then around two corners with high-efficiency turning vanes. The flow is conditioned by a honeycomb flow straightener and fine-mesh screens before entering a contraction from 46 in. \times 46 in. down to the 18 in. \times 18 in. primary test-section inlet.

The secondary stream is driven by a suction-type Cincinnati PB-12A centrifugal fan, which is powered by a 2 h.p. Dayton electric motor. The motor speed is controlled by a Toshiba VF Pack-P transistor inverter. A round-to-rectangular expansion with a honeycomb flow straightener connects the suction pump to the 6.5 in. high by 18 in. wide secondary test-section entrance.

The test section of the shear-layer facility is shown in figure 1. The walls are made out of 1/2 in. clear acrylic for optical access. A 1 in. thick aluminium splitter plate separates the flows over the first 12 in. of the test section. The splitter plate is flat on the primary side and has a contraction over the last 3.5 in. of the secondary side to a tip thickness of approximately 0.4 mm. The top wall of the test section is 1/2 in. thick clear acrylic 36 in. in length and has a pivot allowing for variable upper wall angles relative to the streamwise axis. The bottom wall of the test section has a pivot below the splitter-plate tip. The lower wall consists of flat, 1/2 in. thick, 24 in. long

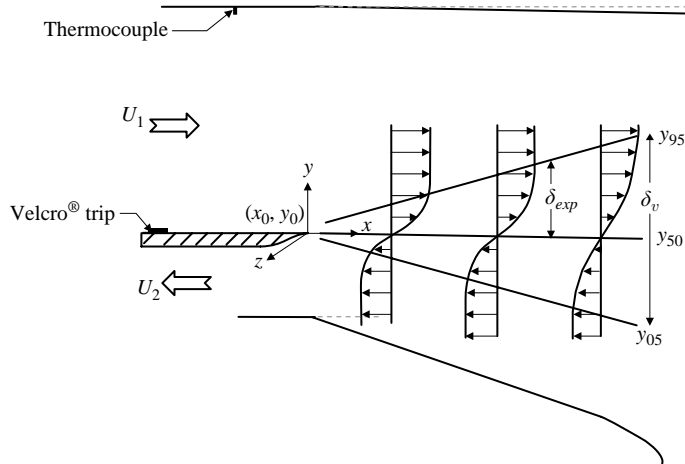


FIGURE 1. Countercurrent shear-layer test-section schematic.

clear acrylic portion with a semi-circular bellmouth ‘entrance’ of 27° of a 18 in. radius circle made of reinforced sheet metal.

The test section is 18 in. in width. The splitter tip is the origin for the streamwise (x) and transverse (y) coordinates, and the spanwise (z) axis is coincident with the splitter-plate trailing edge. The upper and lower tunnel walls have static pressure taps in the midspan plane spaced at 2 in. intervals in the streamwise direction. Identical surfaces without pressure taps were used during PIV data collection to enable improved optical access. The wind tunnel has static pressure taps upstream and downstream of the contraction used to indicate the primary stream velocity. The secondary stream velocity is monitored with a static pressure tap mounted on the flat portion of the lower wall 3 in. upstream (relative to the primary flow) of the splitter-plate tip. Additional hardware details can be found in Tang (2002).

Hot-wire measurements were used to locate the streamwise location where self-similarity is reached. With this information at hand, detailed measurements were made in the self-similar region using PIV. Laskin nozzle aerosol generators were used to create the olive oil droplets used as tracer particles predominantly in the sub-micron range (Gerbig & Keady 1985). A Continuum Surelite II-10 Nd:YAG dual-head laser system produced beams at a wavelength of 532 nm that were transformed into a thin light sheet using a -50 mm cylindrical lens and a 1000 mm spherical lens. A 45° angled mirror directs the sheet to the test section where the beam waist of approximately 0.113 mm occurs.

The PIV system used a TSI model 610032 synchronizer to control the timing of the various elements of the PIV system. The lasers were fired in succession to create two light sheets closely spaced in time. The light scattered off the seeded particles is captured by a TSI Model 630046 cross-correlation camera with a maximum aperture of $f = 2.8$. A frame-grabber card transfers the digital images from the camera to the host computer. The images were captured and processed using TSI’s Insight[®] software version 2.0.

3.1. Preliminary observations

High primary stream velocities were desirable to achieve self-similarity at a reasonable streamwise distance, thus creating a region of self-similarity that could be carefully examined using PIV. To evaluate the quality of the primary flow stream near the

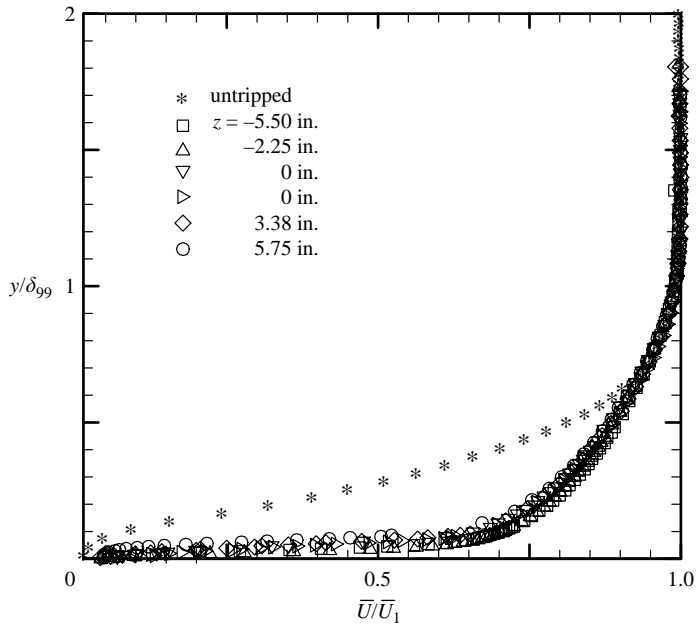


FIGURE 2. Boundary-layer profiles near the splitter-plate trailing edge.

maximum tunnel speed of 32 ms^{-1} , the facility was run in a single-stream shear-layer configuration with the lower tunnel wall removed to allow free entrainment of ambient air. A hot-wire positioned at the centre of the primary stream was used to capture time records to compute the power spectral density of the background flow disturbances. The power spectra indicated low-amplitude peaks associated with the fan blade passage frequency (these peaks were monitored carefully throughout the study, and were consistently absent above the natural disturbances in the shear layer itself). The free-stream turbulence level was consistently below 0.15 % of the primary velocity based on the streamwise velocity component integrated over a frequency range of 1 Hz to 5 kHz.

The uniformity of the primary stream was investigated for the simplified single-stream configuration. A vertical velocity profile was taken with the hot-wire probe in the midspan plane. A spanwise profile was also taken at the centre of the transverse dimension. Both traces showed that the velocity varied somewhat across the test section, but the maximum difference in the cross-stream and spanwise directions was less than 1 % of the mean value outside the thin boundary layers. Further details of the wind-tunnel benchmarking are found in Tang (2002).

With the hot-wire probe positioned in the midspan plane, a vertical profile was taken to measure the boundary layer at the splitter-plate tip. The boundary layer had a thickness of $\delta_{99} = 0.33 \text{ cm}$ and a shape factor of $H = 2.52$, which corresponds to a Reynolds number of $Re_\theta = 790$. The normalized velocity profile is shown in figure 2 as the ‘untripped’ data. An exploration of the existing shear-layer data tends to suggest that a turbulent boundary layer may lead to a shorter streamwise distance to achieve similarity (Mehta & Westphal 1986; Bell & Mehta 1990). Furthermore, a turbulent boundary layer can help minimize facility-dependent initial conditions that may pervade the results. With a suitably tripped boundary layer, the background disturbances are found to be more broadband than the disturbances in the laminar

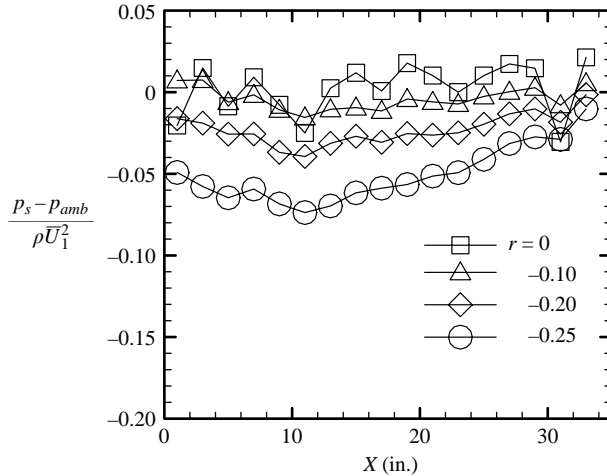


FIGURE 3. Upper wall static pressure profiles.

setting. In addition, if variation appears in the span initially, measurements may need to be spanwise averaged (Bell, Plesniak & Mehta 1992).

A Velcro[®] strip was glued 12 in. upstream of the splitter-plate trailing edge to trip the boundary layer. The Velcro is 1 in. wide and 1/16 in. thick with a cross-hatching pattern to the bristles, which are spaced about 1/64 in. apart. A profile was run for the tripped boundary layer at the splitter-plate tip in the same spanwise location as for the laminar case (at the midspan, $z = 0.0$ in.). The boundary-layer profiles are shown in figure 2. The tripped boundary layer had a thickness of $\delta_{99} = 1.10$ cm with a shape factor of $H = 1.49$ and $Re_{\theta} = 2230$. These results indicate that the tripped boundary layer was indeed fully developed. The Velcro trip was left in place and the spanwise uniformity of the boundary layer was then examined. Splitter-plate-tip boundary-layer profiles were run at five evenly spaced locations across the span. These profiles are also shown in figure 2. The average shape factor of the profiles is $H = 1.52$.

Both the upper and lower walls of the facility have the ability to be deflected in an attempt to remove any streamwise pressure gradients that may exist. First, the upper wall was kept flat while the angle of the lower wall was adjusted downwards. The primary stream was held fixed at 31 m s^{-1} and pressure traces were taken at each lower wall position for counterflow levels from 0% to 25%. The results indicated a general need for a larger lower wall deflection angle with increased counterflow, which is intuitive as a shear layer should grow more rapidly with increased shear. There was, however, a significant cross-stream pressure gradient.

A Pitot-static survey of the secondary stream showed a drop in total pressure over the downstream half of the lower wall along the streamwise direction. Although the primary flow was not physically attached to the lower tunnel wall, it was determined that the shear layer was close enough to the lower wall to have an impact on the total pressure of the secondary stream. The basic conclusion from this rudimentary study is that the distance from the bottom of the shear layer to the lower wall at the secondary stream entrance should be at least of the order of the shear layer width at that point. Once a fixed lower-wall deflection was chosen, a similar study was performed for the upper wall. A constant upper-wall deflection of -0.8° was deemed adequate for all of the counterflow cases, as static pressure traces in figure 3 show minimal streamwise pressure variation, suggesting nominally constant primary stream

velocities. The velocity difference between the two streams is held constant to within 2% over the streamwise region where the self-similar characteristics were explored. The final orientation of the upper and lower tunnel walls are shown in figure 1.

It is well established that hot-wire probes are inherently unsuitable for measuring the velocity in flows that experience significant reverse velocities and high local turbulence levels, both of which are present in the countercurrent shear layer. While a careful examination of the shear layer was not possible using hot wires, their ease of operation rendered the hot-wire probe very useful for determining the approximate streamwise location of the onset of self-similarity at each velocity ratio studied.

Because of the limitations of hot wires in such a complex flow, PIV was employed to measure complete velocity fields. A minimum of 500 image pairs were acquired to limit the uncertainty of low-order turbulent statistics. Each image is divided into interrogation regions; adjacent interrogation regions are overlapped by 50% in order to increase spatial resolution while satisfying the Nyquist criterion. For the present study, the Gaussian sub-pixel approximation function was chosen as it has been found to yield the lowest bias error for the present PIV system (Forliti, Strykowski & Debatin 2000).

An aperture setting of $f = 2.8$ with slight defocusing was chosen, and the peak-locking bias error is estimated to be 0.015 pixels, or 0.25% of the maximum displacement. An additional error is due to window bias, a manifestation of particle clipping on the edges of the interrogation region. The estimated window bias error is 0.02 pixels for the 64×64 case and 0.06 pixels for the 32×32 case. Details of the peak-locking and window bias studies can be found in Tang (2002). The precision error of the mean velocity calculations using 500 images (i.e. samples) in the middle of a shear layer can be estimated using the streamwise turbulence as the variance. The precision error of the mean velocity is approximately 1.6% for the single-stream shear layer. Precision error of the standard deviation (e.g. u'_{rms}) is approximately 6%.

4. Results and discussion

While a careful examination of the shear layer was not possible using hot wires, their ease of operation rendered the hot-wire probe very useful for determining the approximate streamwise location of the onset of self-similarity for each velocity ratio. Typically linear spatial growth of the layer is used as the lowest-order statistic necessary to justify self-similarity. The local length scale of the shear layer is usually based on characteristics of the entire layer (e.g. momentum thickness, pitot thickness, or vorticity thickness), but this was not reasonable from hot-wire data owing to the reverse flow and high local turbulence levels, so a modified experimental thickness, δ_{exp} , was defined for this purpose. The experimental thickness is based on the width of the layer between the 95% upper boundary and the 50% 'middle' of the layer. Note that the x % location, denoted y_x , is the vertical position where the mean velocity \bar{U} is equal to $\bar{U}_2 + x(\bar{U}_1 - \bar{U}_2)$. The advantage of employing δ_{exp} was that it could be measured accurately with the hot-wire probe for all velocity ratios.

Figure 4 shows the mean velocity profiles of the single-stream shear layer measured with the hot-wire probe for a range of distances downstream of the splitter plate. U_2 was assumed to be zero for the single-stream shear-layer case. This leads to an apparent positive secondary stream velocity. This is mostly due to the hot wire capturing an entrainment velocity that is low-speed and likely to be nearly perpendicular to the primary flow. This has been noted in a number of studies of single-stream shear layers (e.g. Liepmann & Laufer 1947).

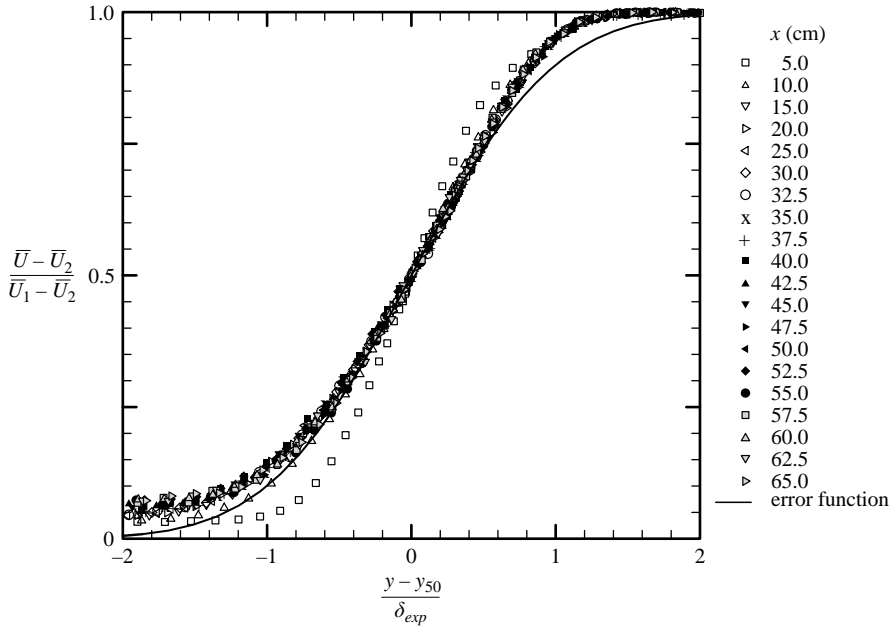


FIGURE 4. Mean streamwise velocity profiles for the single-stream shear layer ($\lambda = 1.0$) obtained using a hot-wire probe.

The single-stream mean velocity profiles appear to collapse at streamwise distances greater than 15 cm downstream of the splitter plate. Figure 4 also shows how the normalized mean profiles compare to a least-squares-fit error function. It is clearly seen that the error function is not a good representation of the shape of the single-stream shear layer. In fact, it does a rather poor job of approximating the edges of the shear layer. The comparison to the error function highlights the asymmetry in the mean velocity profile of the single-stream shear layer.

In the most stringent sense of the word, a flow is self-similar only when the higher-order turbulent terms collapse when normalized by local quantities (Townsend 1976). The fluctuating velocity measured by the hot-wire probe for the single-stream shear layer was normalized by the velocity difference in the free streams and plotted versus the normalized position. Figure 5 shows that the turbulence profiles do ultimately collapse, but at a larger streamwise distance compared to the mean profiles. The collapsed profiles are fairly smooth with slight asymmetry about the shear-layer centre with a peak value shifted slightly towards the high-speed side. This is in good agreement with the numerous single-stream shear-layer studies (e.g. Liepmann & Laufer 1947; Yule 1971) with a possible exception being the peak value.

Based upon a visual inspection of the hot-wire measurements, the turbulent profile for the single-stream shear layer (i.e. $r = 0$) attains self-similarity at a distance of approximately 37.5 cm downstream of the splitter-plate tip, clearly a subjective interpretation. An alternative way of looking at the turbulence self-similarity is the streamwise distance where the peak turbulence intensity asymptotes to a constant value (Bradshaw 1966).

A similar procedure is followed for the cases with counterflow. A comprehensive summary of the hot-wire profiles used to establish the onset of self-similarity can be found in Tang (2002). Results of the hot-wire study regarding the approximate

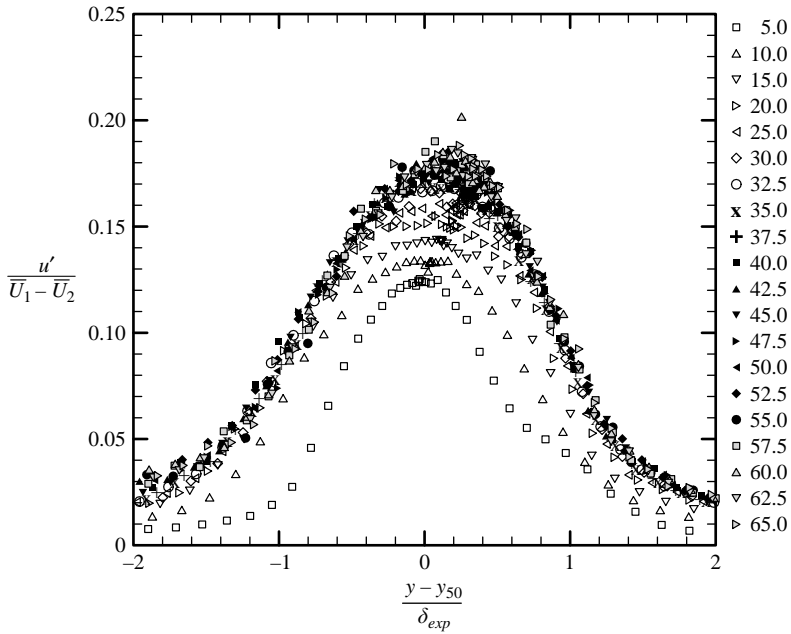


FIGURE 5. Root mean square streamwise velocity fluctuation profiles for the single-stream shear layer ($\lambda = 1.0$) obtained using a hot-wire probe.

r	x_0/θ_0	y_0/θ_0	x_{sp}/θ_0
0.00	33.3	-2.7	286
-0.09	35.5	-3.4	220
-0.13	34.2	-3.7	200
-0.19	-6.8	0.8	241
-0.24	-5.7	0.8	218
-0.29	-2.7	0.5	215

TABLE 1. Summary of shear-layer similarity characteristics.

locations of self-preservation onset (x_{sp}) as well as virtual origins (x_0, y_0) are shown in table 1. The momentum thickness θ_0 for the primary stream at the splitter-plate trailing edge is equal to 0.12 cm.

PIV for each velocity ratio was begun at the streamwise location where self-similarity was established based on the hot-wire surveys. Multiple overlapping domains were required to cover the height of the shear layer as well as to satisfy the optical requirements of the PIV diagnostic. Three domains were patched together for the streamwise width and three or four domains were patched together for the transverse height, the latter needed for shear layers experiencing high spatial growth. The patched domains allow for the entire shear layer width to be quantified and possess enough streamwise measurements to determine growth rates and self-similar velocity profiles.

To gain a qualitative sense of the structures present in the countercurrent shear layer, PIV data were taken in the developing region where the entire shear layer is sufficiently thin to be captured by a single image. The camera was positioned at a streamwise location of $x = 10$ cm. This was estimated to be the farthest downstream region where

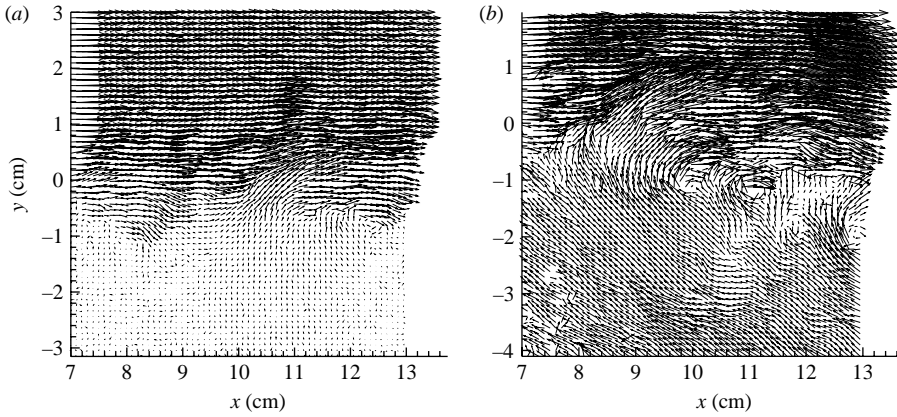


FIGURE 6. Representative instantaneous velocity vector fields in the developing region. (a) $r=0$, $\lambda=1.0$; (b) $r=-0.3$, $\lambda=1.86$.

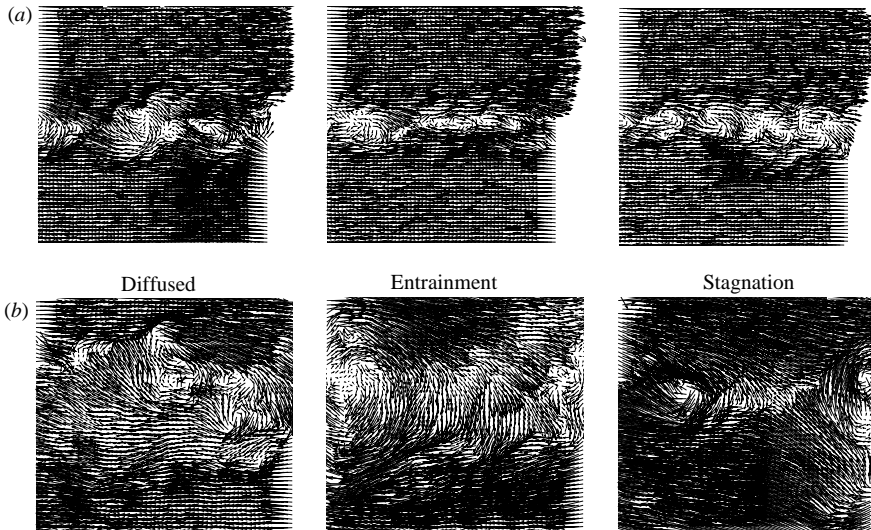


FIGURE 7. Instantaneous velocity vector fields in the convecting reference frame for (a) $r=0.0$ and (b) $r=-0.30$.

the camera could capture the entire shear-layer height for all counterflow levels. This region was chosen to examine shear-layer structure and hence was positioned upstream of the self-similarity region; 100 image pairs were captured for each of the six velocity ratio cases. Figure 6 shows a comparison of representative instantaneous velocity fields for the single-stream and 30% counterflow cases seen in the reference frame stationary with respect to the splitter plate. Flow structures were apparent in all images captured, but there is no indication of the classic coherent structures seen by Brown & Roshko (1974). The tripped boundary layer appears to have removed any dominant coherence. Although no 'clean' structure was observed in the velocity fields, it can be seen that the mixing region is much thicker for the case with counterflow.

To examine this further, random images were studied in the convective reference frame. Figures 7(a) and (b) show three representative instantaneous velocity fields

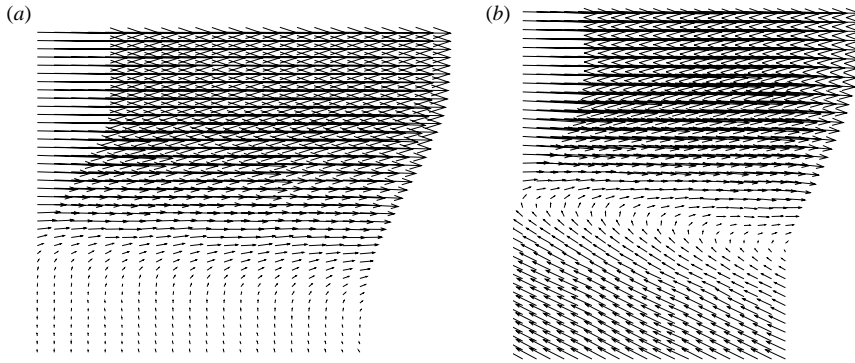


FIGURE 8. Mean velocity vector fields for (a) $r=0$, $\lambda=1.0$ and (b) $r=-0.30$, $\lambda=1.85$.

for the single-stream and 30% counterflow cases. The estimated convective velocity, $U_c = (U_1 + U_2)/2$, has been subtracted from the entire velocity field such that the structures can be seen more clearly. The structures are confined to a relatively narrow transverse region for the single-stream shear layer ($r=0.0$) compared to the considerable domains for the high counterflow case ($r=-0.3$). This is striking, given that the same physical location was selected to compare the two flows. It is clear, however, that multiple scales are present. This location roughly corresponds to the onset of *mean* field self-similarity for all cases as found in the hot-wire study.

The qualitative behaviour observed in the high counterflow vector fields seem to fall into three broad types of activity. Several vector fields show what appears to be a fairly thick mixing region between the two high-speed streams. Large scales that span the entire mixing zone (like those observed by Brown & Roshko) are not present. The velocity magnitudes in the mixing region are low in this reference frame. The second qualitative feature that was observed in many of the vector fields is intense large-scale entrainment. In this state, there appears to be an instantaneous bulk mass exchange between the two streams, in the case shown in figure 7, the flux is from the upper stream to the lower stream. Although subjective, we can see evidence of a large-scale vortical structure present on the left-hand side of the middle vector field in figure 7(b). The third feature often observed in the set of vector fields shows a strong interaction that suggests the two streams are forming a stagnation point. A clear stagnation point can be seen in the right most vector field of figure 7(b). Each vector field obtained for this case fell into one of these three broad categories, although some vector fields contained features of more than one state.

With these qualitative features as a background, we can re-examine the single-stream shear-layer vector fields and observe that some of these same features seem to exist, albeit on a smaller scale. The single-stream shear layer is approximately half as thick as the two-stream shear layer, thus the dynamic features will scale accordingly. Although the vector fields for the two cases seem to be quite different, the basic qualitative features appear to be present in both cases.

Before proceeding with a detailed description of the mean and turbulent characteristics of the countercurrent shear layer, it is necessary to address the facility-dependent nature of the flow. Figure 8 shows the mean vector fields for the single-stream shear layer and 30% counterflow cases. These data are taken in the downstream region where the hot-wire results suggest the flow should be self-similar. Only a small number of the vectors are shown for clarity. The single-stream shear layer shown

in figure 8(a) is seen to spread with downstream distance as expected. The vectors on the low-speed side have very small magnitudes, but it can be seen that they are oriented vertically towards the high-speed stream owing to the induced entrainment flow caused by the shear-layer mixing. The lower wall was removed for this case, as it would have influenced the entrainment process of the shear layer and rendered the results strongly facility dependent.

The 30% counterflow mean vector field shown in figure 8(b) shows the angled secondary flow caused by the orientation of the lower wall (see figure 1). This was deemed necessary in order to generate a secondary flow that has constant pressure and accommodates the large spreading rate of the countercurrent shear layer. Large shear-layer spreading rates imply high levels of mass entrainment, hence a vertical component in the secondary stream will be required to match the entrainment needs of the shear layer. This is clearly one of the fundamental differences between countercurrent and high coflowing shear layers.

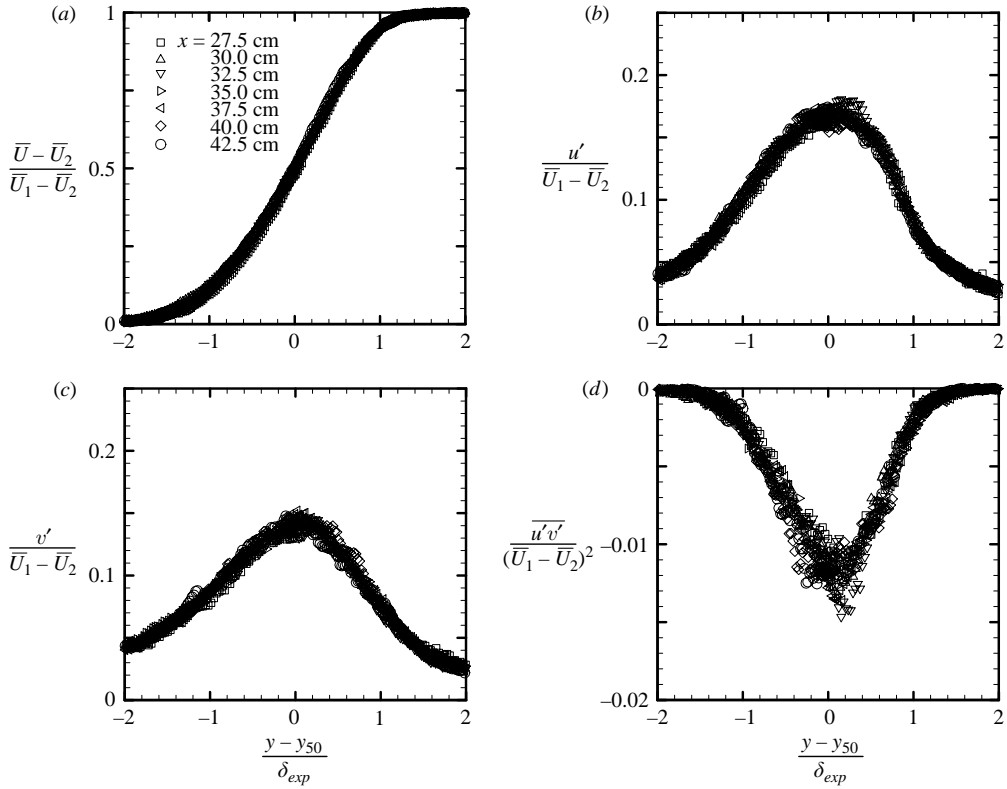
Traditionally, the velocity ratio is defined using the free-stream u -velocity component; however, because of the orientation of the velocity vectors in the secondary stream, an alternative definition of the velocity ratio was also employed. This modified velocity ratio is based on the momentum of the respective streams, and is calculated from:

$$\lambda^* = \frac{|U_1| + |U_2|}{|U_1| - |U_2|}. \quad (4.1)$$

Equation (4.1) is only valid for countercurrent shear layers (the signs in the numerator and denominator are switched for coflowing layers). The difference is that the free-stream velocities U_1 and U_2 have been replaced by the velocity magnitudes of the streams. The primary stream deflection was small, so the difference between λ and λ^* is driven by the magnitude of the transverse velocity in the secondary stream. The difference between λ and λ^* is 3% at $r = -0.3$. From this point on, λ values reported for the PIV results will actually be based on λ^* .

Figure 9 shows the mean and fluctuating velocity profiles using normalized variables for the intermediate counterflow case of $r = -0.19$. The patched measurement domain consists of 163 cross-stream profiles; only seven profiles were plotted for clarity. The transverse distance is normalized by the local experimental thickness δ_{exp} . The mean streamwise velocity profiles in figure 9(a) have clearly attained similarity and collapse very well. Figures 9(b) and 9(c) show reasonable collapse of the data, although scatter has increased relative to the mean velocity profiles. Figure 9(d) shows the Reynolds stress profiles for this case, and shows increased scatter as expected for higher-order statistics. Similar plots for each velocity ratio were used to establish the location where self-similarity begins, which is slightly downstream of the upstream edge of the PIV measurement domain and is governed typically by the high-order quantities. However, with the exception of a small region in the upstream portion of the PIV measurement range, the shear layer has attained a self-preserving state for all six counterflow cases. For growth rate and turbulence statistics comparisons, only the values in the similarity region will be considered.

Since the experimental thickness only accounts for the high-speed half of the shear layer, a different measure of shear-layer thickness was desired that is based on the full velocity profile. The vorticity thickness was recommended by Brown & Roshko (1974) because it is based on the magnitude of shear, which is the driving force behind the mixing. The error function was fit to the mean profiles between the 40% and 60% velocity lines, where the data tend to match the error function shape (see figure 4).

FIGURE 9. Mean and r.m.s. fluctuating velocity profiles for $r = -0.19$.

Unlike the hot-wire data, the PIV velocity profiles are accurate and uncontaminated by local turbulence intensity effects, so a least-squares fit was employed to find the spreading parameter σ used to define the similarity variable

$$\eta = \frac{\sigma(y - y_{50})}{x - x_0}, \quad (4.2)$$

that is based on the formulation

$$\frac{\bar{U} - \bar{U}_2}{\bar{U}_1 + \bar{U}_2} = \frac{1}{2} + \frac{1}{2} \operatorname{erf}(\eta). \quad (4.3)$$

This is the analytical solution for a fully developed shear layer using a simple eddy-viscosity turbulence model (e.g. Schlichting 1979). The spreading parameter is inversely proportional to the shear-layer growth rate. Once the spreading parameter is found, it can be related to the vorticity thickness growth rate

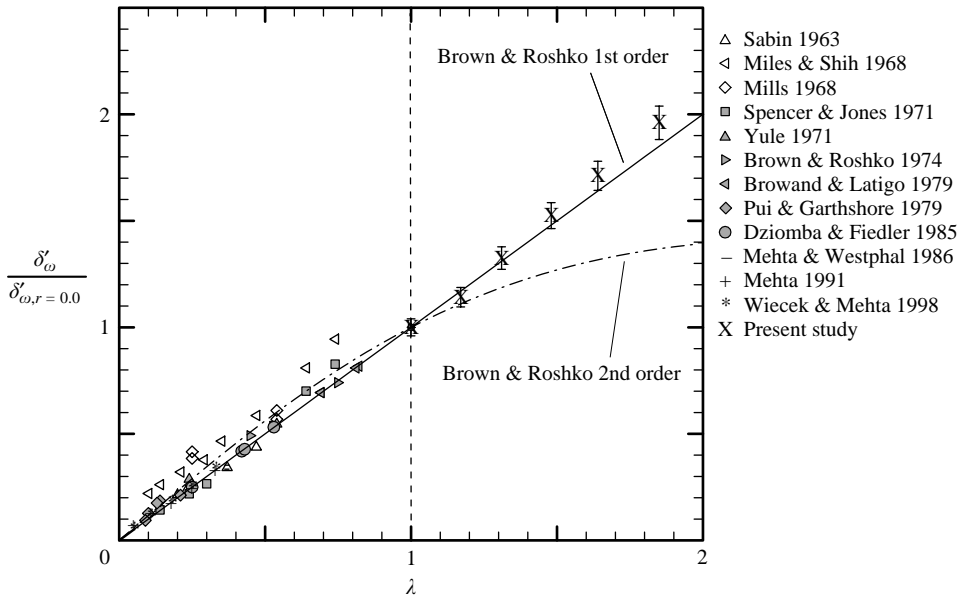
$$\delta'_\omega = \frac{d\delta_\omega}{dx} = \frac{\sqrt{\pi}}{\sigma} \quad (4.4)$$

for the error function velocity profile. The vorticity thickness is defined as

$$\delta_\omega = \frac{\bar{U}_1 - \bar{U}_2}{\left(\frac{d\bar{U}}{dy}\right)_{\max}}. \quad (4.5)$$

r	λ	x/θ_0	$d\delta_{exp}/dx$	$d\delta_\omega/dx$	σ	$u'_{max}/\Delta\bar{U}$	$v'_{max}/\Delta\bar{U}$	$-\overline{u'v'}_{max}/\Delta\bar{U}^2$
0.00	1.00	>319	0.080	0.144	12.27	0.157	0.120	0.00874
-0.08	1.17	>255	0.094	0.165	10.75	0.158	0.120	0.00958
-0.13	1.31	>234	0.109	0.191	9.29	0.16	0.124	0.00949
-0.19	1.48	>234	0.120	0.220	8.05	0.175	0.146	0.01288
-0.24	1.64	>213	0.137	0.247	7.17	0.186	0.163	0.01447
-0.30	1.85	>213	0.147	0.283	6.26	0.186	0.163	0.01498

TABLE 2. Summary of PIV results.

FIGURE 10. Shear-layer growth rate as a function of velocity ratio λ .

Although the entire profile is not well represented by the error function, the middle portion of the shear layer used in the least-squares fit matches well with the error function shape, hence the technique is an accurate method for calculating the vorticity thickness growth rate, since the maximum velocity gradient falls in this region. Additionally, the vorticity thickness is approximately 1.8 times the experimental thickness, fairly independent of velocity ratio. Table 2 summarizes the various growth rate values for each velocity ratio, as well as peak turbulence statistics and streamwise locations where self-similarity was established.

The vorticity thickness growth rates found for all six cases, as measured with PIV, are shown in figure 10 along with results from literature. The growth rates are normalized by the growth rate of the single-stream shear layer, a method that helps to reduce scatter caused by facility-dependent effects. This is equivalent to the common manner of presenting growth rates in terms of σ_0/σ where σ_0 is the spreading parameter for the single-stream shear layer. Because of the variety of shear-layer thickness definitions used in the research community, some conversions were required for some of the data referenced from other studies. A qualitative examination of the trend seems to indicate a quasi-linear behaviour for data obtained in countercurrent shear layers, i.e. for

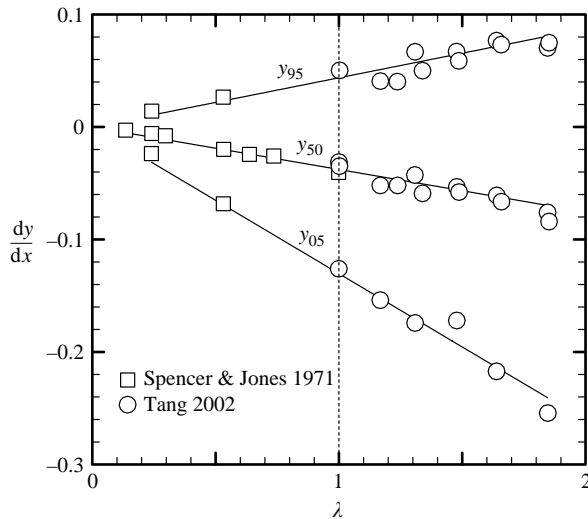


FIGURE 11. Slopes of the iso-velocity lines as a function of λ .

$\lambda \geq 1$. This would correspond to the first-order approximation (linear correlation) of Brown & Roshko (1974). The error bars presented for the present data are associated with uncertainties in the curve-fitting process to obtain the growth rate parameter σ .

The curves on the plot are the first- and second-order growth rate solutions of Brown & Roshko (1974). Both relations reasonably capture the trends for coflowing shear layers, though only the first-order form matches the experimental trend for the countercurrent shear layers. The turbulence statistics presented later will shed further light on the shear-layer development, and, in particular, connections that can be made between the flow response and predictions of the spatio-temporal stability applied to the countercurrent shear layer.

The shear layers grow linearly with the streamwise coordinate in the self-similar regime. Thus, iso-velocity contours will be linear. The slopes of the iso-velocity lines for the 95 %, 50 % and 5 % normalized velocity contours are shown in figure 11 as a function of the normalized velocity ratio. These points represent the edges and mid-point of the shear layer. Also included in the plot are values from the present hot-wire study (at $\lambda = 1$) as well as data from the comprehensive coflowing study of Spencer & Jones (1971). There is a distinct linear trend for all data when the normalized velocity ratio λ is used, an observation that is supported by the generally linear trend of the shear-layer growth rates presented in figure 10. Ideally, more data points would be available, but there appears to be a universal behaviour across all velocity ratios. With these linear fits, the shear-layer location can be approximated for an arbitrary velocity ratio. As has been noted by several workers (e.g. Yule 1971), the shear-layer centreline moves toward the low-speed side as λ is increased. It is worth mentioning that the relationship between r and λ is nonlinear, where modest levels of counterflow (in terms of reverse velocity U_2) produce large changes in the velocity ratio parameter λ .

Figures 10 and 11 are surprising since they show that the shear-layer growth trend is consistent for both coflowing and counterflowing shear layers, yet we expect some change in the flow due to a change in the stability characteristics for $\lambda > 1.315$. We must look in both the mean and fluctuating velocity fields for manifestations of a stability transition. Figure 12 shows peak streamwise turbulence measurements over a range of velocity ratios. With the exception of the present study and Olsen (1999),

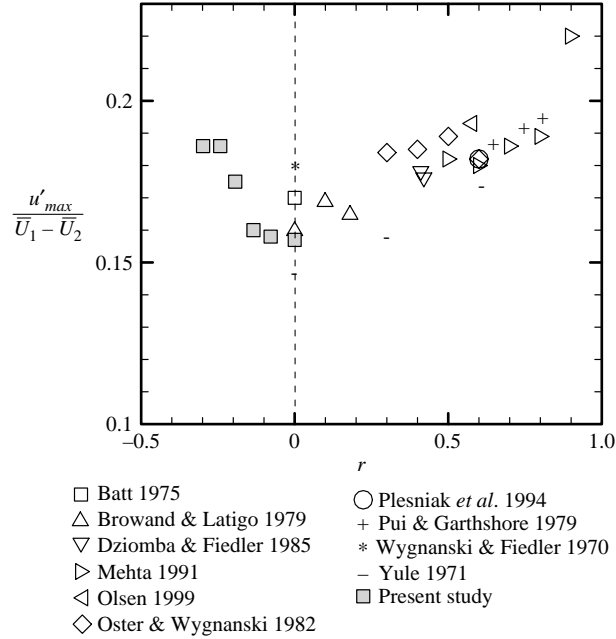


FIGURE 12. Peak r.m.s. streamwise velocity fluctuation levels.

the measurements were made with hot wires. There is large scatter due to facility and measurement differences. The most notable is the single-stream layer where the placement of lower walls and endplates severely alters the entrainment field and has a significant effect on the mixing (Husain & Hussain 1979). Even in the present study with the same facility, a 16% difference was found in the single-stream turbulence level between the two measurement techniques; only results from PIV were included for the present study.

The prevailing trend in the coflowing regime is a decrease in peak turbulence intensity with decreasing velocity ratio r . This is most dramatic at high coflow levels and almost levels off as the single-stream case is approached, although this trend may be contaminated by insufficient self-similarity definition for coflowing shear layers, as wake effects from the trailing edge may yet be present particularly at high levels of coflow. It is hard to decipher the exact trend as very few studies have been conducted at high-coflow levels. In contrast to this trend, the peak turbulence intensity is abruptly increased as r is reduced below -0.13 .

Figure 13 shows the variation of the peak values of the fluctuating velocity components as well as the Reynolds stress and isotropy as a function of velocity ratio for negative r values. The trends are very similar for all quantities shown. It appears that there is an abrupt change in the peak turbulence quantities for counterflow levels above 13%. In addition, the turbulence goes through a transition to higher isotropy suggesting enhanced three-dimensionality. In fact, for the counterflow layers up to $r = -0.13$, $v'_{max}/u'_{max} = 0.76$ but the relation shifts to $v'_{max}/u'_{max} = 0.88$ for the highest two counterflow layers, indicating a transition in the nature of the turbulence between $r \cong -0.1$ and -0.2 .

4.1. Similarity results

The quantity of data collected for each velocity ratio is very high. Once the self-similar region is determined, both the mean and turbulent quantities were collapsed

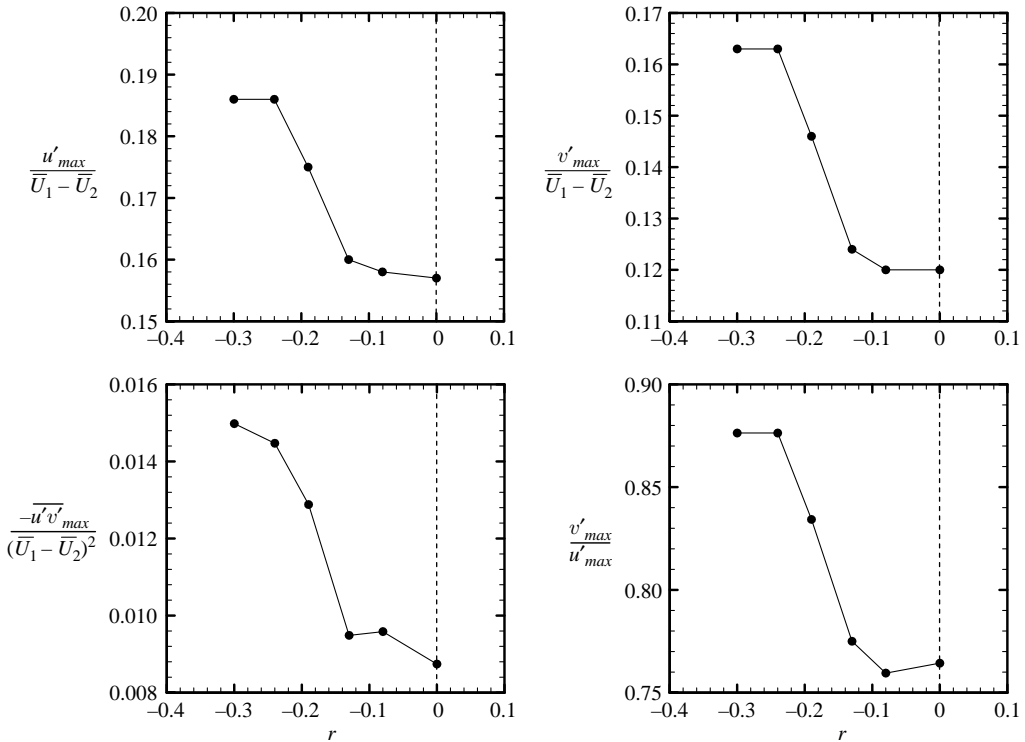


FIGURE 13. Peak fluctuation levels and isotropy as a function of velocity ratio r .

using the appropriate scaling variables, obtaining smooth representations of the self-preserving profiles. This is effectively a streamwise averaging process for the self-similar mean and fluctuating velocity profiles. This allowed for a careful examination of the countercurrent shear-layer characteristics over the range of conditions studied.

Figure 14 presents the self-similar velocity profiles for the single-stream and countercurrent shear layers. Included in the data for reference is the moderately high coflowing velocity ratio ($\lambda = 0.33$) of Mehta (1991) and the error function. It is clear that the Mehta profile tends to agree well with the error function, which is a symmetric profile. For the present study, the velocity profiles have nominally the same shape, although the high counterflow level ($\lambda = 1.85$) shows slight deviation on the low-speed side of the shear layer. Comparing the current results to the Mehta data and the error function, it is clear that shear layers with counterflow or low coflow have a different shape from high coflowing shear layers. It appears that the velocity profile transitions away from a symmetric shape as coflow is decreased.

The conservation of mass can be used to help understand this observation. Assuming two-dimensional self-similar behaviour, the conservation of mass can be used to show

$$\frac{\sigma(\bar{V}_1 - \bar{V}_2)}{\bar{U}_1 - \bar{U}_2} = \int_{-\infty}^{+\infty} f'(\eta)\eta \, d\eta, \quad (4.6)$$

where $f(\eta)$ is the normalized self-similar velocity profile, η is the similarity parameter defined in (4.2), and \bar{V}_1 and \bar{V}_2 are the cross-stream velocities in the two free-streams. The integration in (4.6) becomes zero if the derivative of the velocity profile is symmetric (as is the case for the error function). For shear layers that have strong entrainment, the cross-stream velocity difference is relatively large. This requires the

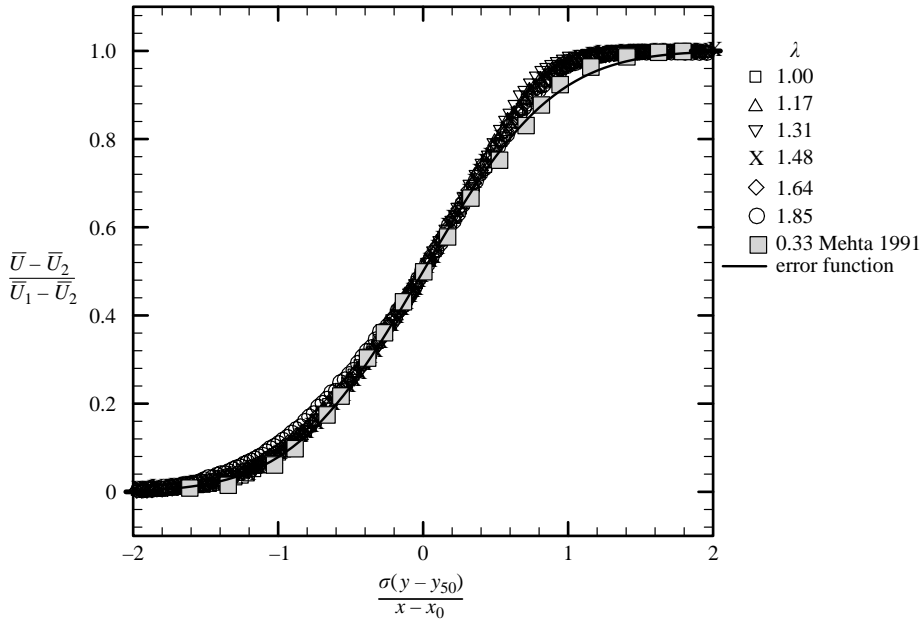


FIGURE 14. Self-similar mean velocity profiles as a function of λ .

derivative of the self-similar velocity profile to be asymmetric, otherwise the integral goes to zero. Hence, for shear layers that have non-zero normalized entrainment, the velocity profile cannot be represented by a symmetric function (such as the error function). The fact that high coflowing shear layers seem to have symmetric velocity profiles suggests negligible induced entrainment in the free streams. Note that strong coflowing shear layers entrain fluid, but do not induce a cross-stream velocity in the free streams because the fast-moving streams naturally flow into the mixing region as the shear layer grows. Equation (4.6) also shows the proportional relationship between shear-layer growth and entrainment.

It is not purely the mean field that determines the turbulent field, but rather a mutual interaction between the two. Figure 15 shows the shapes of the composite streamwise fluctuating velocity profiles (averaged over the region of self-similarity) for the six cases as measured with PIV. The turbulent profiles for the first three cases (namely $\lambda = 1.0, 1.17, 1.31$) overlap very closely. However, the self-similar shape deviates sharply for counterflow levels above $\lambda \sim 1.3$. The trend in the peak values was seen in figure 13, but these profiles show that the increase occurs across the entire shear layer.

The transverse velocity fluctuation and Reynolds stress profiles are shown in figures 16 and 17, respectively. Similar trends can be seen in all turbulent quantities with v'^2 and $\overline{u'v'}$ differences being even more dramatic than in u'^2 . Noting that the shape of the mean velocity contour is nominally invariant, the Reynolds stress profiles are evidence of a fundamental difference in turbulent energy production. For a fixed shear-layer thickness, the turbulent energy production term at 30% counterflow is approximately 75% larger than a single-stream layer with the same driving shear ΔU .

From 0% to 13% counterflow, the turbulent profiles collapse, indicating that there is a common mechanism for generating the turbulence that scales with growth rate and velocity difference ΔU . Above 13% counterflow, there is an increase in all

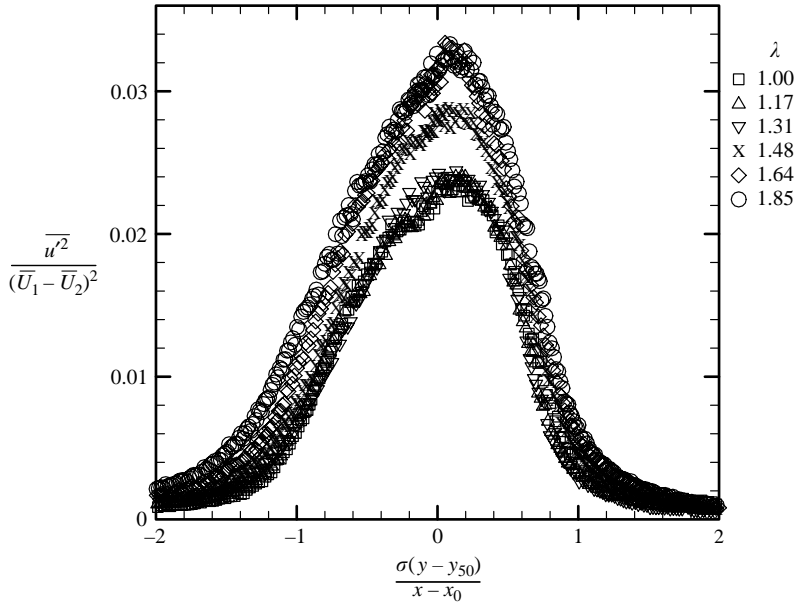


FIGURE 15. Self-similar fluctuating streamwise velocity profiles as a function of λ .

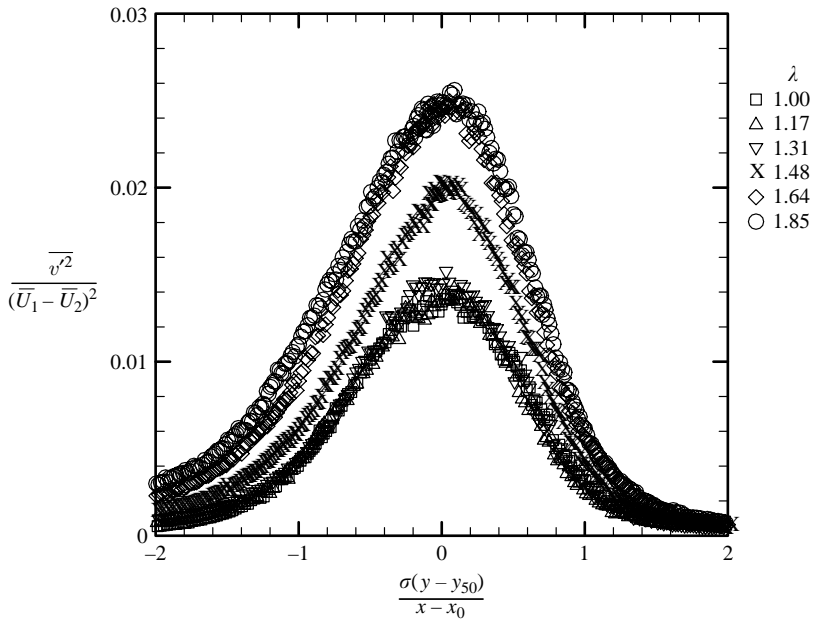
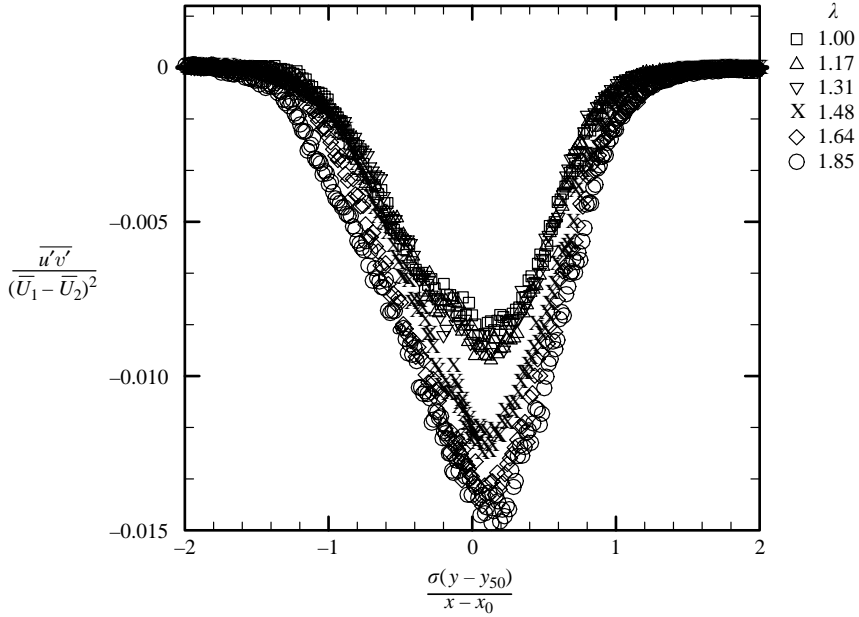


FIGURE 16. Self-similar fluctuating cross-stream velocity profiles as a function of λ .

turbulent transport terms. Since the mean profiles were all nominally similar, there must be an enhanced mechanism for turbulent energy production above approximately $\lambda \sim 1.3$. Coincidentally perhaps, linear stability theory predicts a transition at $\lambda = 1.315$ (Huerre & Monkewitz 1985) for the hyperbolic-tangent function, which is based upon a laminar shear-layer solution. Beyond this critical velocity ratio, non-convecting disturbances are amplified in time, namely the onset of absolute instability is reached.

FIGURE 17. Self-similar Reynolds stress profiles as a function of λ .

The turbulent transport quantities suggest a transition occurring at counterflow levels above approximately 13 %, yet the shear-layer growth appears to be nominally linear over the full range of conditions explored. The momentum and mass conservation equations for the self-similar two-dimensional shear layer give additional insight to these observations. The mean streamwise velocity can be represented as

$$\bar{U} = \Delta U f(\lambda; \eta) + \bar{U}_2, \quad (4.7)$$

which upon substitution into the two-dimensional continuity equation yields an expression for the self-similar mean traverse velocity of

$$\bar{V} = \bar{V}_2 + \frac{\Delta U}{\sigma} \left[\eta f(\lambda; \eta) - \int_{-\infty}^{\eta} f(\lambda; \eta) d\eta \right]. \quad (4.8)$$

These forms can be substituted into the streamwise momentum equation where the boundary-layer approximations have been employed and the viscous terms neglected, namely:

$$\bar{U} \frac{\partial \bar{U}}{\partial x} + \bar{V} \frac{\partial \bar{U}}{\partial y} + \frac{\partial \overline{u'v'}}{\partial y} = 0. \quad (4.9)$$

A self-similar representation for the Reynolds stresses is assumed to follow the form

$$\overline{u'v'} = \Delta U^2 g(\lambda; \eta). \quad (4.10)$$

Note that up to this point no assumption has been made regarding the possible dependencies of the self-similar functions f and g on the velocity ratio λ . Substitution of the above presented forms of \bar{U} , \bar{V} and $\overline{u'v'}$ into the momentum equation results in

$$-\bar{U}_2 \eta f'(\lambda; \eta) + \bar{V}_2 \sigma f'(\lambda; \eta) - \Delta u f'(\lambda; \eta) \int_{-\infty}^{\eta} f(\lambda; \eta) d\eta + \Delta u \sigma g'(\lambda; \eta) = 0. \quad (4.11)$$

An equation analogous to (4.11) is presented in Tennekes & Lumley (1972) for free shear layers. Their analysis is based on a single-stream shear layer assuming a zero mean traverse velocity in the middle of the shear layer.

Two assumptions will be made to advance the analysis. The first assumption is the linear relationship of the growth rate with λ , namely:

$$\frac{1}{\sigma} = \frac{1}{\sigma_0} \frac{\bar{U}_1 - \bar{U}_2}{\bar{U}_1 + \bar{U}_2} = \frac{1}{\sigma_0} \lambda, \quad (4.12)$$

where σ_0 is the spreading parameter for $\lambda = 1$. This assumption is supported by figure 10. The second assumption, based on experimental observation in the present study, is the assumption that the traverse velocity of the high-speed stream \bar{V}_1 is zero. This assumption along with (4.8) yields

$$\bar{V}_2 = -\frac{\Delta U}{\sigma} C_1, \quad (4.13)$$

where C_1 represents the bracketed term in (4.8) to $+\infty$ and is only a function of the mean streamwise velocity similarity function $f(\lambda; \eta)$. Implementing these equations into the momentum equation leads to

$$-\frac{1-\lambda}{2} \eta f'(\lambda; \eta) - \lambda C_1 f'(\lambda; \eta) - \lambda f'(\lambda; \eta) \int_{-\infty}^{\eta} f(\lambda; \eta) d\eta + \sigma_0 g'(\lambda; \eta) = 0. \quad (4.14)$$

At this point, we will assume that the mean streamwise velocity function f is independent of λ , an assumption substantiated by figure 14. Application of this equation at $\lambda = 1$ yields

$$-C_1 f'(\eta) - f'(\eta) \int_{-\infty}^{\eta} f(\eta) d\eta + \sigma_0 g'(\lambda = 1; \eta) = 0, \quad (4.15)$$

an expression that will be used subsequently. In order to explore the sensitivity of the interaction between the mean and turbulent flow fields as a function of the velocity ratio, the derivative of (4.14) with respect to λ results in

$$\frac{1}{2} \eta f'(\eta) - C_1 f'(\eta) - f'(\eta) \int_{-\infty}^{\eta} f(\eta) d\eta + \sigma_0 \frac{\partial g'(\lambda; \eta)}{\partial \lambda} = 0. \quad (4.16)$$

Equations (4.14) and (4.15) can be combined forming

$$\frac{1}{2} \eta f'(\eta) - \sigma_0 g'(\lambda = 1; \eta) + \sigma_0 \frac{\partial g'(\lambda; \eta)}{\partial \lambda} = 0. \quad (4.17)$$

Noting that the two left-hand terms are independent of λ , resulting in

$$\frac{\partial g'(\lambda; \eta)}{\partial \lambda} = \text{constant}, \quad (4.18)$$

a statement that the Reynolds stress profiles change at a linear rate with λ . If we observe the present shear-layer data for $\lambda \leq 1.31$, the constant in (4.18) must be zero since the normalized Reynolds stress profiles are the same. Figure 17 illustrates the fact that the Reynolds stress profiles drastically change for $\lambda > 1.31$, yet the shear layer continues linear growth with respect to λ . It is clear that (4.16) cannot hold for the full range of counterflow cases studied here, since the normalized Reynolds stress profiles collapse up to $\lambda = 1.31$, then increase at higher counterflow levels. The primary assumptions used to derive (4.16) are valid over the full range of conditions, suggesting the departure in the collapse of the turbulence profiles must coincide with a development of three-dimensional mean flow.

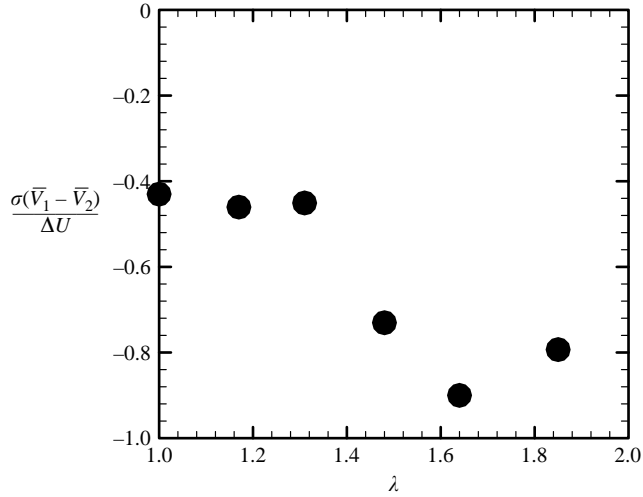


FIGURE 18. Entrainment velocity as a function of velocity ratio λ .

To further explore the issue of three-dimensional mean flow, the measured transverse velocity difference across the shear layer is normalized and is presented in figure 18. The normalized velocity difference for a two-dimensional shear layer is expected to be a constant value based on (4.13). It is clear from the figure that a transition occurs above $\lambda = 1.31$ where significantly higher levels of entrainment occur in comparison to a two-dimensional shear layer with the same spreading rate. Hence, there is abundant evidence that one of the manifestations of the apparent stability transition includes the development of mean flow three-dimensionality. It is suspected that a flow of this nature will typically have a stronger dependence on the experimental configuration. Note that if the flow were to return to a two-dimensional mean flow state in the post-transition regime, the proportional relationship between shear-layer growth and entrainment would force the normalized entrainment velocity to return to the pre-transition level of approximately -0.45 .

5. Conclusions

Spatially developing countercurrent shear layers were examined. An invariant primary velocity of $U_1 = 31 \text{ m s}^{-1}$ was used, and velocity ratios of $r = 0.00, -0.09, -0.13, -0.19, -0.24$ and -0.30 were studied. Hot-wire anemometry was used to gain a qualitative view of the entire flow field and PIV was used to quantify a region of self-preserving flow. Since there is a considerable amount of data on coflowing shear layers, the present results should help add to the existing knowledge such that shear-layer characteristics can be predicted over a very large range of velocity ratios.

The shear-layer growth rate was found to increase with counterflow at a rate nominally predicted by low-order analytical models. The growth rate of a single-stream shear layer was increased by approximately 100% when 30% counterflow was applied, illustrating the nonlinear effect of counterflow (growth is linear in λ). Peak turbulence levels were also increased by up to 30%. Trends for peak turbulence level versus velocity ratio up to $\lambda \sim 1.3$ compared well with previous coflowing studies. However, above a critical velocity ratio of approximately $\lambda = 1.3$, turbulence levels increased.

When properly normalized, mean velocity profiles were found to have a nominally consistent shape regardless of velocity ratio. However, the turbulent profiles were found to change drastically above a critical velocity ratio, which corresponds reasonably well to the transition to absolute instability as predicted by linear stability analysis. It was determined that mean flow three-dimensionality is present for $\lambda > 1.3$.

The present results greatly expand our understanding of countercurrent shear layers and add to the coflowing studies of the past. The basic shape of the mean and turbulent velocity fields was found for countercurrent shear layers, which will be useful as a base for comparing turbulence models, as past models have generally performed poorly in separated flows where counterflow is present. The study was successful in quantifying fully developed countercurrent shear layers and finding a fundamental change in the shear-layer behaviour above a critical level of counterflow.

The transition observed at a critical velocity ratio $\lambda \sim 1.3$ in a self-similar turbulent shear layer is remarkably coincident with predictions from spatio-temporal linear theory where $\lambda_{cr} = 1.315$. The theory indicates the onset of absolute instability when the counterflow level in a planar laminar shear layer exceeds 13.6% of the primary stream. In practice, the presence of locally absolutely unstable flow may lead to global instability. The effect of the skewness of the middle of the shear layer has been found to have no effect on the subsequent analysis and therefore has been neglected.

The authors would like to acknowledge the generous support of the Office of Naval Research under contract N00014-01-1-0644 as well as the guidance they have received from technical monitor Dr Gabriel D. Roy.

REFERENCES

- BATT, R. G. 1975 Some measurements on the effect of tripping the two-dimensional shear layer. *AIAA J.* **13**, 245–247.
- BELL, J. H. & MEHTA, R. D. 1990 Development of a two-stream mixing layer from tripped and untripped boundary layers. *AIAA J.* **28**, 2034–2042.
- BELL, J. H., PLESNIAK, M. W. & MEHTA, R. D. 1992 Spanwise averaging of plane mixing layer properties. *AIAA J.* **30**, 835–837.
- BIRCH, S. F. & EGGERS, J. M. 1972 A critical review of the experimental data for developed free turbulent shear layers. *Free Turbulent Shear Flows Conference*, (NASA SP-321 **1**, 1973), pp. 11–40.
- BRADSHAW, P. 1966 The effect of initial conditions on the development of a free shear layer. *J. Fluid Mech.* **26**, 225–236.
- BROWAND, F. K. & LATIGO, B. O. 1979 Growth of the two-dimensional mixing layer from a turbulent and nonturbulent boundary layer. *Phys. Fluids* **22**, 1011–1019.
- BROWN, G. L. & ROSKHO, A. 1974 On density effects and large structure in turbulent mixing layers. *J. Fluid Mech.* **64**, 775–816.
- DRAZIN, P. G. & REID, W. H. 1981 *Hydrodynamic Stability*. Cambridge University Press.
- DZIOMBA, B. & FIEDLER, H. E. 1985 Effect of initial conditions on two-dimensional free shear layers. *J. Fluid Mech.* **152**, 419–442.
- FORLITI, D. J., STRYKOWSKI, P. J. & DEBATIN, K. 2000 Bias and precision errors of digital particle image velocimetry. *Exps. Fluids* **28**, 436–447.
- GERBIG, F. T. & KEADY, P. B. 1985 Size distributions of test aerosols from a Laskin nozzle. *Microcontamination*, July, 56–61.
- HO, C. M. & HUERRE, P. 1984 Perturbed free shear layers. *Annu. Rev. Fluid Mech.* **16**, 365–424.
- HUERRE, P. & MONKEWITZ, P. A. 1985 Absolute and convective instabilities in free shear layers. *J. Fluid Mech.* **159**, 151–168.
- HUMPHREY, J. A. C. & LI, S. 1981 Tilting, stretching, pairing, and collapse of vortex structures in confined countercurrent flow. *J. Fluids Engng* **103**, 466–470.

- HUSAIN, Z. D. & HUSSAIN, A. K. M. F. 1979 Axisymmetric mixing layer: influence of the initial and boundary conditions. *AIAA J.* **17**, 48–55.
- KHEMAKHEM, A. S. D. 1997 An experimental study of turbulent countercurrent shear layers. PhD thesis, University of Minnesota – Twin Cities, Minneapolis, MN.
- LIEPMANN, H. W. & LAUFER, J. 1947 Investigations of free turbulent mixing. *NACA TN* 1257.
- MEHTA, R. D. 1991 Effect of velocity ratio on plane mixing layer development: influence of the splitter plate wake. *Exps. Fluids* **10**, 194–204.
- MEHTA, R. D. & WESTPHAL, R. V. 1986 Near-field turbulence properties of single- and two-stream plane mixing layers. *Exps. Fluids* **4**, 257–266.
- MILES, J. B. & SHIH, J. S. 1968 Similarity parameter for two-stream turbulent jet-mixing region. *AIAA J.* **6**, 1429–1431.
- MILLS, R. D. 1968 Numerical and experimental investigations of the shear layer between two parallel streams. *J. Fluid Mech.* **33**, 591–616.
- OLSEN, M. G. 1999 Planar velocity measurements in an incompressible and a weakly compressible mixing layer. PhD thesis, University of Illinois at Urbana–Champaign, Urbana IL.
- OSTER, D. & WYGNANSKI, I. 1982 The forced mixing layer between parallel streams. *J. Fluid Mech.* **123**, 91–130.
- PLESNIAK, M. W., MEHTA, R. D. & JOHNSTON, J. P. 1994 Curved two-stream turbulent mixing layers: three-dimensional structure and streamwise evolution. *J. Fluid Mech.* **270**, 1–50.
- PUI, N. K. & GARTHSHORE, I. S. 1979 Measurements of the growth rate and structure in plane turbulent mixing layers. *J. Fluid Mech.* **91**, 111–130.
- RAMSHANKAR, R. 1988 The dynamics of countercurrent mixing layers. PhD thesis, Yale University, New Haven CT.
- RODI, W. 1975 A review of experimental data of uniform density free turbulent boundary layers. *Studies in Convection*. Academic Press.
- SABIN, C. M. 1963 An analytical and experimental study of the plane, incompressible, turbulent free shear layer with arbitrary velocity ratio and pressure gradient. PhD thesis, Stanford University, Palo Alto, CA.
- SCHLICHTING, H. 1979 *Boundary-Layer Theory*, 7th edn. McGraw–Hill.
- SPENCER, B. W. & JONES, B. G. 1971 Statistical investigation of pressure and velocity fields in the turbulent two-stream mixing layer. AIAA Paper 71–613, *AIAA 4th Fluid and Plasma Dyn. Conf.*
- STRYKOWSKI, P. J. & NICCUM, D. L. 1991 The stability of countercurrent mixing layers in circular jets. *J. Fluid Mech.* **227**, 309–343.
- STRYKOWSKI, P. J. & NICCUM, D. L. 1992 The influence of velocity and density ratio on the dynamics of spatially developing mixing layers. *Phys. Fluids A* **4**, 770–781.
- STRYKOWSKI, P. J. & WILCOXON, R. K. 1993 Mixing enhancement due to global oscillations in jets with annular counterflow. *AIAA J.* **31**, 564–570.
- TANG, B. A. 2002 An experimental investigation of planar countercurrent turbulent shear layers. MS thesis, University of Minnesota, Minneapolis, MN.
- TENNEKES, H. & LUMLEY, J. L. 1972 *A First Course in Turbulence*. MIT Press.
- THORPE, S. A. 1968 A method of producing a shear flow in a stratified fluid. *J. Fluid Mech.* **32**, 693–704.
- THORPE, S. A. 1971 Experiments on the instability of stratified shear flows: miscible fluids. *J. Fluid Mech.* **46**, 299–319.
- TOWNSEND, A. A. 1976 *The Structure of Turbulent Shear Flow*. Cambridge University Press.
- WIECEK, K. C. & MEHTA, R. D. 1998 Effects of velocity ratio on mixing layer three-dimensionality. *Exps. Thermal Fluid Sci.* **16**, 165–176.
- WILCOXON, R. K. 1996 Mixing enhancement in an axisymmetric jet with annular counterflow. PhD thesis, University of Minnesota, Minneapolis, MN.
- WYGNANSKI, I. & FIEDLER, H. E. 1970 The two-dimensional mixing region. *J. Fluid Mech.* **41**, 327–361.
- YULE, A. J. 1971 Two-dimensional self-preserving turbulent mixing layers at different free stream velocity ratios. *Aero. Res. Council Rep. Mem.* 3683.